

# JGR Solid Earth

## RESEARCH ARTICLE

10.1029/2021JB022116

### Key Points:

- We present a high-resolution 3-D velocity model of the Tengchong volcano (TCV) using ambient noise adjoint tomography
- We reveal a multi-level magma system in TCV, that is, a low velocity zone in the uppermost mantle feeds the crustal magma reservoir
- The lower crustal basaltic magma reservoir has a volume of  $\sim 7,000 \text{ km}^3$  at depths of 20–35 km with melt fraction of  $\sim 2\%$ –4.5%

### Supporting Information:

Supporting Information may be found in the online version of this article.

### Correspondence to:

Z. Guo,  
[guoz3@sustech.edu.cn](mailto:guoz3@sustech.edu.cn)

### Citation:

Zhao, Y., Guo, Z., Wang, K., & Yang, Y. J. (2021). A large magma reservoir beneath the Tengchong volcano revealed by ambient noise adjoint tomography. *Journal of Geophysical Research: Solid Earth*, 126, e2021JB022116. <https://doi.org/10.1029/2021JB022116>

Received 25 MAR 2021

Accepted 11 JUN 2021

## A Large Magma Reservoir Beneath the Tengchong Volcano Revealed by Ambient Noise Adjoint Tomography

Y. Zhao<sup>1,2</sup>, Z. Guo<sup>2,3,4</sup> , K. Wang<sup>5</sup>, and Y. J. Yang<sup>5</sup>

<sup>1</sup>Harbin Institute of Technology, Harbin, China, <sup>2</sup>Department of Ocean Science and Engineering, Southern University of Science and Technology, Shenzhen, China, <sup>3</sup>Shanghai Sheshan National Geophysical Observatory, Shanghai, China, <sup>4</sup>Southern Marine Science and Engineering Guangdong Laboratory (Guangzhou), Guangzhou, China, <sup>5</sup>ARC/Centre of Excellence for Core to Crust Fluid System and GEMOC ARC National Key Centre, Earth and Planetary Sciences, Macquarie University, Sydney, NSW, Australia

**Abstract** The Tengchong volcano (TCV) is a large active volcano system in the southeastern Tibetan Plateau. It is characterized by large-volume magmatic gas emission, active hydrothermal circulation, and intense volcanic and earthquake activities, posing a threat of near future eruptions. However, there is still no available model of the magmatic plumbing system beneath the volcano system, limiting the quantitative assessments of the eruption hazards. Here, we present a high-resolution 3D model of the TCV constructed using ambient noise adjoint tomography. Our 3D model reveals a large basaltic magma reservoir with a volume of  $\sim 7,000 \text{ km}^3$  at depths of 20–35 km, which has a melt fraction of  $\sim 2\%$ –4.5%. Our results suggest that the deep crustal magma reservoir is fed by partial melting in the uppermost mantle and is recharging the shallow magma chambers beneath the TCV. Our results are key to understanding the volcanic activities and assessing future eruption hazards.

**Plain Language Summary** The Tengchong volcano (TCV) is one of the largest active intraplate volcanoes in southwest China. The unrests of the TCV in recent years have attracted a lot of attention and aroused concerns for the future explosive eruptions. In this study, we present a high-resolution 3D model of the TCV using an innovative method of ambient noise adjoint tomography. Our results reveal a multi-layered magmatic plumbing system in the lower crust and uppermost mantle beneath the TCV. The large basaltic magma reservoir in the lower crust has a volume of  $\sim 7,000 \text{ km}^3$  at depths of 20–35 km and melt fraction of  $\sim 2\%$ –4.5%. Thus, the total of melt volume reaches  $140\text{--}315 \text{ km}^3$ . The deep crustal magma reservoir is fed by partial melting in the uppermost mantle and is recharging the shallow magma chambers. If such a large volume of melt gets erupted in the future, the lava could cover a huge area, threatening the livelihood of the half million people living nearby. It, therefore, becomes urgent to quantitatively assess and model the potential of future eruptions.

## 1. Introduction

The Tengchong volcano (TCV), situated in the west of the southeastern Tibetan Plateau, is one of the largest active volcanoes in China (Figure 1a). The TCV is characterized by large-volume magmatic gases ( $\text{CO}_2$  and sulfide) emission (C. P. Zhao et al., 2011, 2012), active hydrothermal circulation (Jiang et al., 2019), high surface heat flow ( $\geq 90 \text{ mWm}^{-2}$ ), intensive earthquake (Zhang & Lei, 2015; Y. Zhao et al., 2020) and volcanic activities (Y. Wang et al., 2007; Zou et al., 2014) during the Holocene. There are 68 volcanic centers distributed in the Tengchong Block. The activities of the TCV can be divided into four stages (Jiang, 1998; Y. Wang et al., 2007): the late Miocene-Pliocene basalt (5.5–4.0 Ma), the Pliocene-Pleistocene olivine-basaltic rocks (3.8–0.9 Ma), the Pleistocene andesites and dacites (0.8–0.1 Ma), the late Pleistocene-Holocene trachybasalts, basaltic trachyandesites, and trachydacites (0.1–0.01 Ma). The most recent volcanic eruption occurred at AD1609 (Zhao, 2008).

A Tengchong Volcanic Geothermal National Geological Park was established in 2001, featuring volcanic fields and hydrothermal activities of the TCV. Since then, the national park becomes a popular tourist destination and attracts a large number of tourists. In addition, there are nearly half a million people living within 30 km of the volcanoes. The unrests of the TCV with intense seismicity, geothermal activities, and emission of magmatic gases have attracted a lot of attention and aroused concerns for the future explosive

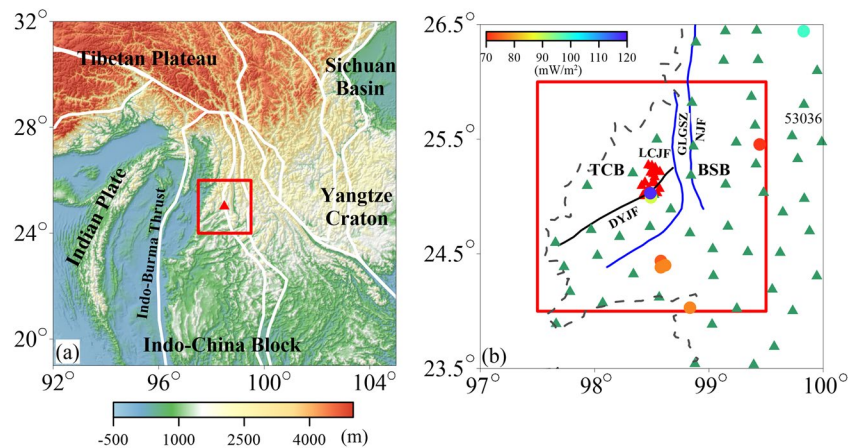


**Figure 1.** (a) Tectonic units of the Tengchong volcano region. The white lines outline the boundaries between major blocks. The red box outlines the study region. The red triangle shows the location of Tengchong volcano. (b) The red box also delineates the map region in Figure 6. The black lines and blue lines indicate major faults. The dark-gray dash line is the borderline of China. The green triangles represent the 52 seismic stations, and the red triangle shows the locations of volcanoes. The colored dots are the heat flow observations taken from Jiang et al. (2019). Abbreviations stand as follows: BP, Burma Plate; ICB, Indo-China Block; GLGSZ, Gaoligong Shear Zone; TCB, Tengchong Block; BSB, Baoshan Block; DYJF, Dayingjiang Fault; LCJF, Longchuanjiang Fault; NJF, Nujiang Fault; HNF, Huna Fault.

eruptions. Assessing potential volcanic hazards call for a more quantitative study of the magma plumbing system of the TCV.

The TCV (Figure 1a) is situated ~600 km to the east of the Indo-Burma Thrust, where the Burma slab subducts beneath the southwestern Tibet. The north-south trending Gaoligong Shear Zone (GLGSZ), bounded by the Nujiang Fault (NJF) and Longchuanjiang Fault (LCJF), separates the Tengchong Block (TCB) from the Baoshan Block (BSB, Figure 1b) (B. Zhang et al., 2012). Previous geological and geophysical studies suggest that the volcanic eruption of the Tengchong was largely controlled by these deep-rooted strike-slip faults, such as NJF and LCJF (Y. Wang et al., 2007). Recent seismic tomography studies (Huang et al., 2019) reveal a plume-like mantle upwelling beneath the TCV that can be traced down to the mantle transition zone, suggesting a deep origin of the TCV. Magnetotelluric survey reveals three small separated shallow magma chambers at 10–20 km depths beneath the TCV (Ye et al., 2018). However, it still remains enigmatic how deep upper mantle upwelling interacts with the shallow magmatic system and whether there exists a deep crustal magma reservoir that charges the shallow magma chambers, controlling the eruptions of the TCV.

Ambient noise tomography has become a routine technique to obtain high resolution crustal and upper mantle velocity structure (Shapiro et al., 2004). However, traditional methods ignore the complex wave propagation phenomena in 3-D media, such as the effects of elevation on the wave propagation (Guo et al., 2016; Li et al., 2018; Shapiro et al., 2004; Yang et al., 2007; Yao et al., 2008). Such limitations of ray-theory based methods make it hard to accurately image the magma system of the TCV where the variations of elevation are significant. Ambient noise adjoint tomography, which involves solving 3D seismic wave equation in the presence of variations in elevation, is capable of constraining velocities beneath volcanic areas more accurately (Chen et al., 2014; Gao & Shen, 2014; Tape et al., 2009; Tromp et al., 2005, 2010; K. Wang et al., 2019), thus helping improve the quantitative estimation of the melt fraction in the crustal magmatic system.

In this study, we present a refined 3-D crustal and uppermost mantle model of the TCV constructed by ambient noise adjoint tomography using 5–40 s vertical-component Rayleigh waves. Our aim is to image the crustal magmatic system and estimate the melt fraction and speculate on the upwelling path of magma from uppermost mantle to crust beneath the TCV.

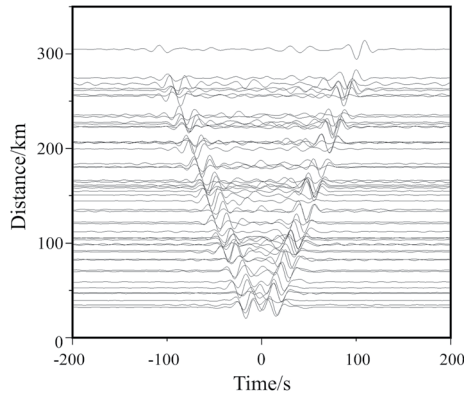


**Figure 2.** Ambient noise cross correlations between the station 53,036 and all other stations.

## 2. Data and Methods

We collect seismic ambient noise recorded by a total of 52 temporary broadband seismic stations from the ChinArray-Himalaya I (Ding & Wu, 2013) deployed in the southeastern Tibet between April 2011 and December 2013. We follow the ambient noise data processing procedures that are presented by Bensen et al. (2007) to obtain vertical-component cross-correlations (Figure 2) at the period band of 5–40 s between all station pairs. The data processing procedures are briefly described as follows: first, raw continuous data recorded at each station are cut into daily segments and decimated to 1 Hz; then, they are band-pass filtered at period band between 5 and 40 s; afterwards, daily seismogram segments are whitened at time and spectral domain; finally, we cross correlate and linearly stack all the daily correlations between station pairs to obtain final cross-correlation (Figure 2). Finally, we further stack the positive and negative segments of each cross-correlation to obtain the symmetric cross-correlation functions.

The empirical Green's function (EGF)  $G_{1,2}(t)$  between a station pair is derived from the negative time derivative of the symmetric cross-correlation function  $C_{1,2}(t)$  (e.g., Snieder, 2004; Yao & Van Der Hilst, 2009) as

$$-\frac{dC_{1,2}(t)}{dt} \approx G_{1,2}(t) \quad (1)$$

We employ the ambient noise adjoint tomography method (Chen et al., 2014; Liu et al., 2017; K. Wang et al., 2018, 2019; C. Zhang et al., 2018) to construct the high resolution 3D S-wave velocity model of the Tengchong volcanoes by iteratively fitting observed EGFs with synthetic Green's functions (SGFs). The adjoint tomography technique has been well described by numerous previous studies (Fichtner et al., 2010; Luo, 2012; Tromp et al., 2005). Therefore, we here give a brief introduction of kernel calculations and the optimization method.

Traveltime adjoint tomography seeks to minimize the traveltime misfit between observed and synthetic waveforms. The variation of the misfit  $\delta\phi$  is linearly related to the model perturbations via

$$\delta\phi = \int (K_\rho \delta \ln \rho + K_{V_S} \delta \ln V_S + K_{V_P} \delta \ln V_P) d^3 \mathbf{x}, \quad (2)$$

where  $K_\rho, K_{V_S}, K_{V_P}$  are the sensitivity kernels with respect to the density  $\rho$ , shear wave velocity  $V_S$ , and compression wave velocity  $V_P$ . The sensitive kernels  $K(x)$  are calculated by the adjoint method which can be expressed (Tromp et al., 2005; K. Wang et al., 2018) as:

$$K(x) = u(x, t; x_s) \otimes u^\dagger(x, T - t; x_r), \quad (3)$$

where  $u(x, t; x_s)$  is the forward wavefield generated by the sources, and the adjoint wavefield  $u^\dagger(x, T - t; x_r)$  is computed by time-reversed adjoint sources emitted from receivers. The operator  $\otimes$  represents the time integration of interaction between the forward and adjoint wavefields.

All event kernels are summed, and smoothed with a 3D Gaussian function to obtain the misfit gradient  $\mathbf{g}$ . Table S1 lists the size of each Gaussian function used in each iteration. In adjoint tomography, we do not calculate the Hessian matrix due to the high computational cost. Instead, we use a pre-conditioner to approximate the Hessian matrix and the model is updated by the negative preconditioned misfit gradient:

$$\delta \mathbf{m} \sim -\mathbf{P}^{-1} \mathbf{g} \quad (4)$$

$\mathbf{P}$  is the pre-conditioner which can be found in (K. Wang et al., 2018; Zhu et al., 2015). The step length for model updating is determined by a line search method (Zhu et al., 2015).

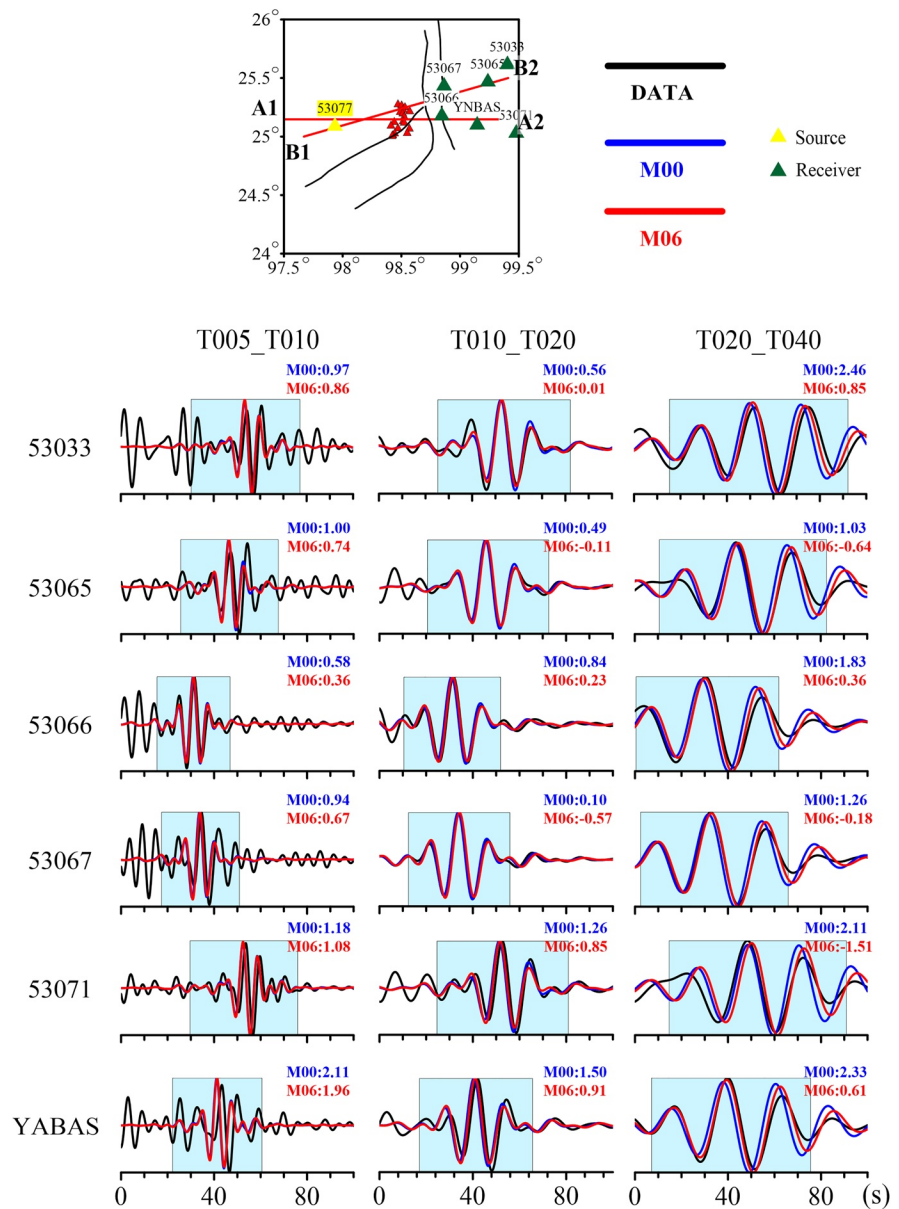


**Figure 3.** Waveform fitting between observed waveforms and synthetics in three different bands. The yellow and green triangles represent a source of station 53,077 and receivers, respectively. The three columns display waveform fitting of each receiver at the three different bands. All the waveforms shown here have the common source of station 53,077, and the receiver for waveforms in each row are indicated in the left. Traveltime misfits are shown with corresponding colors. The sky-blue boxes are the sizes of windows for traveltime misfit measurement.

The SGFs of Rayleigh waves are simulated using the spectral element method (SEM) with a 3-D velocity model (Komatitsch & Vilotte, 1998; Tromp et al., 2008). The initial shear wave velocity model (M00) is extracted from Zheng et al. (2016), which is constructed by jointly inverting surface wave dispersions and receiver functions. The SEM mesh in this study is constructed using the meshing tool of SPEC-FEM3D\_Cartesian. Two interfaces are honored in the mesh, including the topography derived from the ETOPO1 data (Amante & Eakins, 2009) and a buffer layer. The buffer layer is a smoothed version of topography to dampen mesh distortions resulting from the dramatic terrain (Lee et al., 2008). The domain is divided into two subregions: from the bottom of the mesh to the buffer layer (12 layers), and the buffer layer to the surface (1 layer). So, in total, there are 13 layers in the domain. The element size is doubled beneath the buffer layer, which has lower velocities near the surface compared to velocities of the layers at greater depths



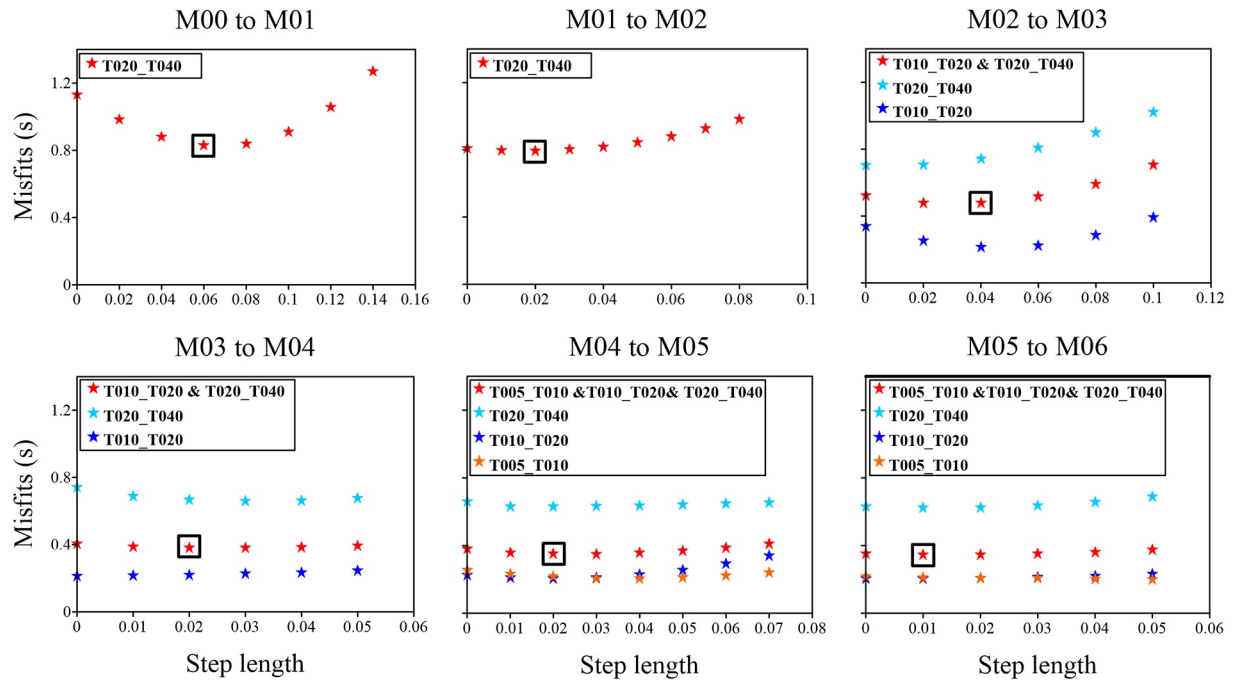


**Figure 4.** Line searches for model updating. Misfits from different period bands are plotted by colored stars as specified in the legend boxes, with the red ones representing mean values of existing period band(s). The black box indicates the optimal step length.

(K. Wang et al., 2018). The mesh (97°E–100°E and 23.5°N–26.5°N) has 144 elements in both longitude (306 km) and latitude (333 km). The average element size of the mesh is about 3 km which can accurately simulate seismic waves down to a period of 4 s. Here, we only present the region of interest (red box in Figure 1b), which covers the whole TCV. A vertical point-force source with a Gaussian source time function of 1 s half duration is injected at the surface beneath each station to simulate the SGFs.

Following K. Wang et al. (2018), EGFs and SGFs are both filtered to three period bands (5–10, 10–20, and 20–40 s). An amplitude normalization is applied to all the EGFs with the maximum of corresponding SGFs' amplitudes. A time window of  $[D/U_{\max} - T/2, D/U_{\min} + T/2]$  is utilized to isolate Rayleigh waves for measuring the frequency-dependent phase traveltimes misfits between the EGFs and SGFs based on the multi-taper technique (Tape et al., 2010; Zhou et al., 2004) (Figure 3). Here,  $D$  is the interstation distance,  $T$  represents the maximum period of individual period bands, and  $U_{\max}$  and  $U_{\min}$  are the maximum and minimum group velocities measured by a frequency-time analysis method (Bensen et al., 2007; Levshin & Ritzwoller, 2001). A set of window selection parameters to control the fit quality between data and synthetics at each iteration are listed in Table S1. We have a total of 1,326 EGFs for all stations and we only retain EGFs with signal-to-noise ratios (SNR) > 30 and interstation distances longer than the one wavelength (Luo et al., 2015; K. Wang et al., 2018). Furthermore, the parameters of time shift  $dT$  and cross-correlation coefficient criteria  $CC_{\min}$  are getting tighter over iterations. Thus, finally we have 850, 1095, 900 measurements at the three periods of 5–10 s, 10–20 s, and 20–40 s, respectively. A final misfit function is calculated by averaging the misfits of the existing bands for all traveltimes measurements, and is related to model perturbations through the interaction between the forward and adjoint simulations (Liu & Tromp, 2006; Tromp et al., 2005) (Equations 2 and 3).

We iteratively refine the 3-D model ( $\rho$ ,  $V_p$ , and  $V_s$ ) through a preconditioned gradient-based method by minimizing traveltimes misfits between the EGFs and SGFs (Chen et al., 2014) (Equation 4). Given the weak sensitivities of Rayleigh waves to density, we scale the relative perturbation of density to 0.33 of the  $V_s$  perturbations (Chen et al., 2014; Montagner & Anderson, 1989). We use all the data set with a line-search method to determine the step length over iterations for model updating (Figure 4 and Table S2). The inversion terminates when the misfit reduction between the last two iterations becomes less evident (Figure 5).

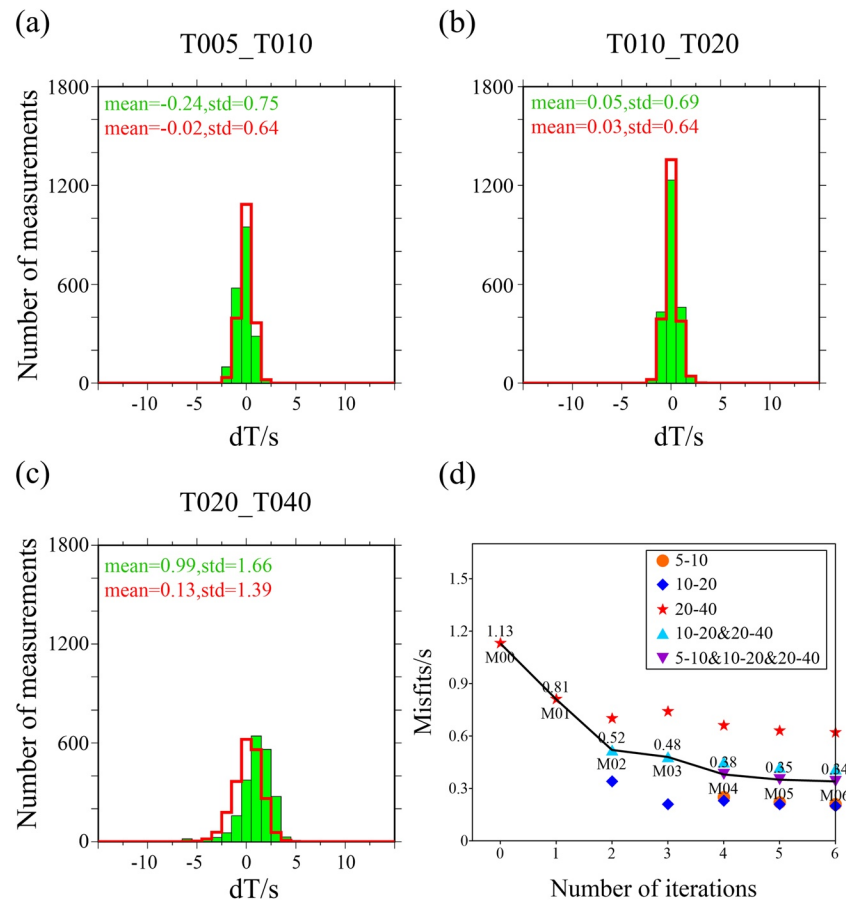


**Figure 5.** (a–c) Histograms of traveltime misfits in different bands for model M00 (green) and M06 (red). The number of measurements used in inversion, average and standard deviation of misfits are also listed above the histograms with the corresponding color. (d) Overall misfit curve decreases over six iterations. The misfits at each frequency band are represented by colored symbols as shown in the legend box.

We start the inversion with the initial model (M00) to firstly fit the long-period band, and gradually introduce measurements made at the short-period bands over six iterations to obtain the optimal model (M06).

### 3. Results

#### 3.1. 3-D Seismic Velocity Model

Our 3-D S-wave velocity ( $V_s$ ) model from ambient noise adjoint tomography is shown as slices at various depths in Figure 6. The predominant feature of our model is a significant low shear velocity zone (LVZ) with a minimum velocity  $\leq 3.25$  km/s in the mid-to-lower crust. The LVZ is located slightly to the west of the TCV (Figures 6 and 7), and is bounded by the Dayingjiang Fault (DYJF) and Longchuanjiang Fault (LCJF) to the south and east of the volcano, respectively. The LVZ becomes horizontally elongated at depths below 20 km. In the uppermost mantle, widespread low velocities (3.85–3.9 km/s) are observed to the east of the Tengchong, particularly along the GLGSZ at the depth of 50 km.

To better visualize the vertical changes of the LVZ, we present two cross-sections (locations shown in Figure 6c) down to the depth of 60 km in Figure 7. These two profiles transect the TCV, the GLGSZ, and BSB. Both profiles display an ellipsoid-shaped LVZ at a depth range of 20–35 km, located slightly to the west of the TCV, with the most prominent velocity reduction of  $\sim 9\%$  relative to the regionally averaged velocity occurring at  $\sim 30$  km depth. In the uppermost mantle (40–50 km), a larger-scale LVZ is observed with the LVZ body slightly shifted to the east of the volcanoes. In addition, 1D shear wave velocity ( $V_s$ ) profiles of our

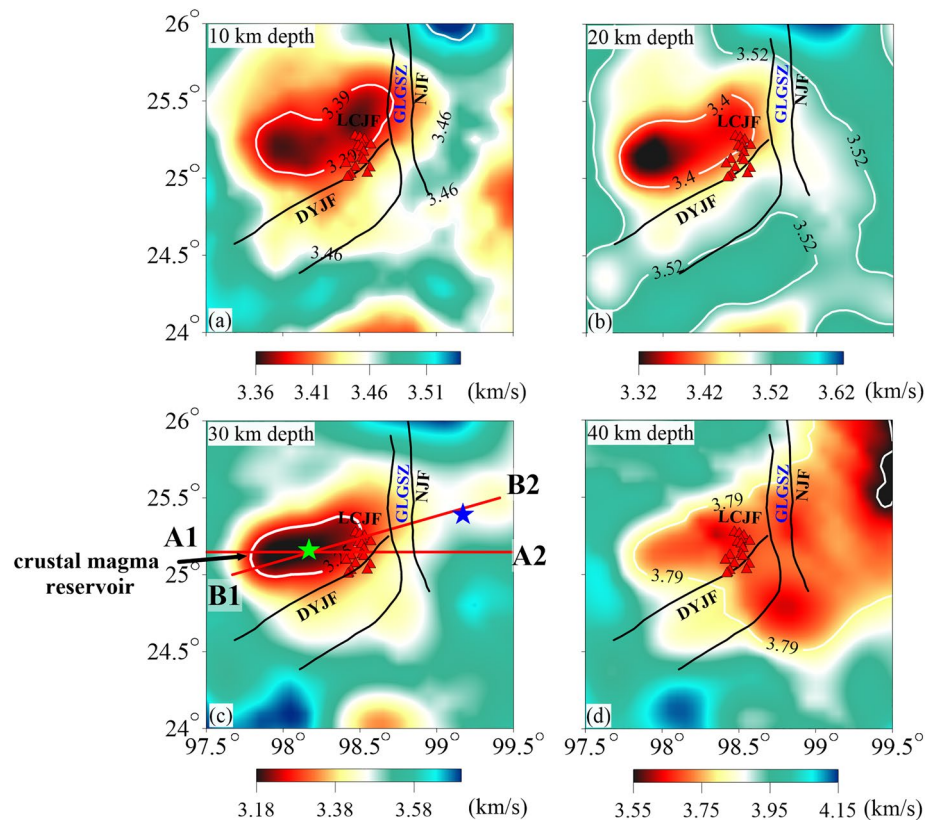


**Figure 6.** Maps showing shear wave velocity at depths of 10–40 km. The red triangles represent the volcanoes. The black lines indicate major faults, and the white lines are contours. Map (c) showing the locations of two profiles (A1A2–B1B2) represented by red lines and 1-D profiles marked with colored stars for two points in Figure 7.

model (Figure 7a) show that the Tengchong Block (TCB) region (the green star) has a marked LVZ at 30 km depth with Vs reaching as low as 3.15 km/s. We also find that Vs of the uppermost mantle ( $\sim 45$  km) beneath the BSB (the blue star) is very low, with the minimum Vs reaching 3.80 km/s. The strong Vs reductions in the mid-to-lower crust of TCB and the uppermost mantle of BSB indicate partial melting must exist at these depths, calling for an estimate of melt fraction.

### 3.2. Resolution Test

We conduct resolution tests to evaluate the model resolution of the adjoint tomography. In the checkerboard resolution test (Figure 8), the velocity anomaly has a lateral dimension of  $0.5^\circ \times 0.5^\circ$  at depths from 0 to 60 km with only lateral velocity perturbation of  $\pm 10\%$  relative to the 1-D regionally averaged velocity model of M00. We conduct synthetic waveforms simulation and adjoint tomography using the same station-pairs as the real data inversion. The synthetic waveforms are computed using the perturbed model. We filter the synthetic waveforms at the three same period bands as input data for resolution tests, and the inversions start from the 1-D regional average model of M00. The workflow of synthetic inversion and the method to choose parameters are the same as the real data inversion. The recovered model is plotted in Figure 8a2–8d2. Because the northwestern corner of the study region is outside the border of China and lacks station coverage, the recovered model here is not well imaged from the checkerboard resolution test. However, the main features of most regions can be recovered, especially at depths of 20 and 30 km. For 40 and 50 km depths of checkerboard resolution test, the amplitude of anomaly is generally underestimated.

Furthermore, to further verify that the mid-to-lower crustal LVZ is a robust feature and to test the vertical resolution of the adjoint tomographic model, a custom resolution test (Figure 9) is carried out with a cuboid-shaped low velocity anomaly set at depths between 20 and 35 km to the east of Tengchong volcanoes.

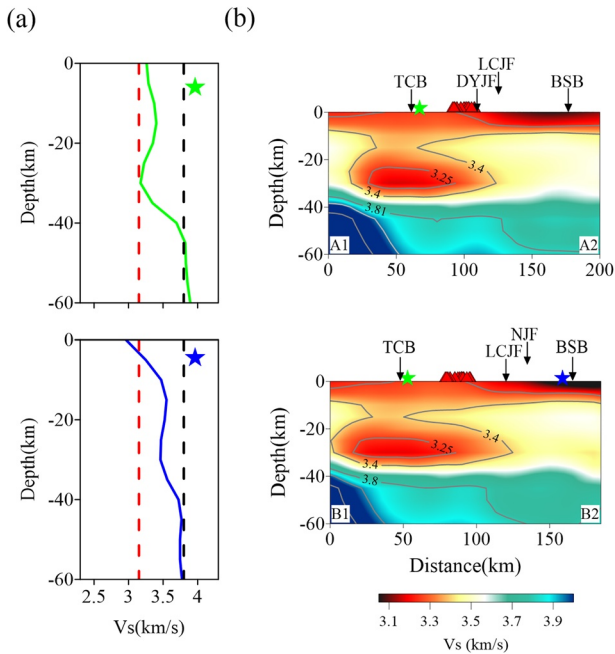


**Figure 7.** (a) 1-D profiles of shear wave velocity for two points as shown in Figure 6c marked by different color stars. The red and black dash line represent Vs values of 3.15 and 3.8 km/s, which are the lower bounds of mid-to-lower crustal and uppermost LVZs, respectively. (b) Cross-sections of shear wave velocity along two profiles shown in Figure 9c for final model (M06). The red triangles are the locations of the volcanoes.

The velocity decrease is 10% relative to the 1-D regional average model of M00 with a lateral size of  $0.64^\circ \times 0.52^\circ$ . The spatial distribution and geometry of the low velocity are similar to the observed LVZ. The recovered velocity model (Figure 9a2–9b2) from the custom resolution test shows that the main feature of input low velocity anomaly can be well recovered by the adjoint tomography.

## 4. Discussions

### 4.1. Melt Fraction of the Low Velocity Zone

Crustal xenoliths found in the Baoshan Block suggest that the lower crust of the study region is dominant by mafic granulite (Ji et al., 2000). In the normal mid-to-lower crust, mafic granulite has a typical shear velocity of 3.82 km/s at 0.6 GPa (Christensen, 1996), indicating that the observed crustal LVZ ( $\leq 3.25$  km/s) has a velocity reduction of at least 0.57 km/s. A recent geochemical study suggests that basaltic magma temperature is around 1,000°C at depths of 20–40 km beneath the TCV (Hu et al., 2018; Yu et al., 2010). In order to estimate the melt fraction of the LVZ, we need to first estimate how much of the velocity reduction originates from an elevated temperature. In doing so, we use shear-velocity-vs-temperature coefficients ( $-dV_s/dT$ ) that are given by a series of end-number rocks from felsic to ultra-mafic rocks ( $1.39\text{--}3.93 \times 10^{-4}$  km/s°C) (Kern & Richter, 1981) to estimate the thermal contribution to velocity variation. Based on these coefficients, a high temperature of 1000°C in the middle/lower crust can account for a velocity reduction of 0.13–0.39 km/s, suggesting that partial melting should be invoked to explain the remaining Vs reduction. In the calculation, we use values for a two-phase meidum consisting of mafic granulite and basaltic melt system at a temperature of 1000°C and pressure of  $\sim 0.6$  GPa ( $\sim 25$  km) (details can be found in

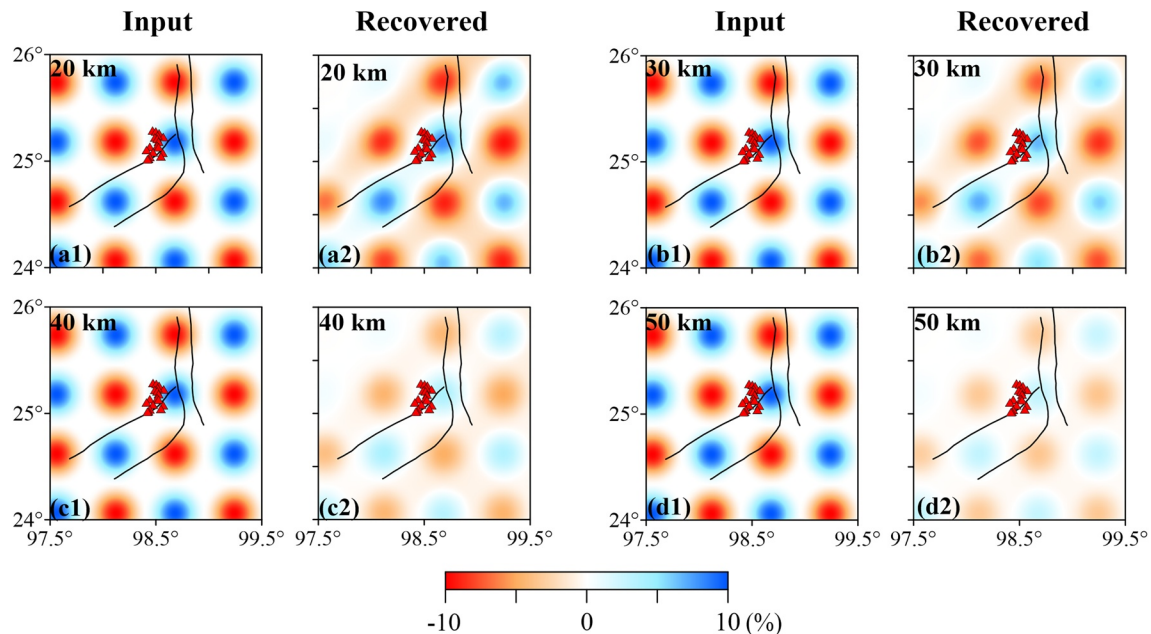


**Figure 8.** Checkerboard resolution test. The input model (a1–d1) is checkerboard style velocity  $\pm 10\%$  anomalies relative to the 1-D regional velocity model of M00 with lateral size of  $0.5^\circ \times 0.5^\circ$ . a2–d2 shows anomalies recovered by our adjoint tomography. The red triangles are the locations of the volcanoes, and black lines represent the major faults.



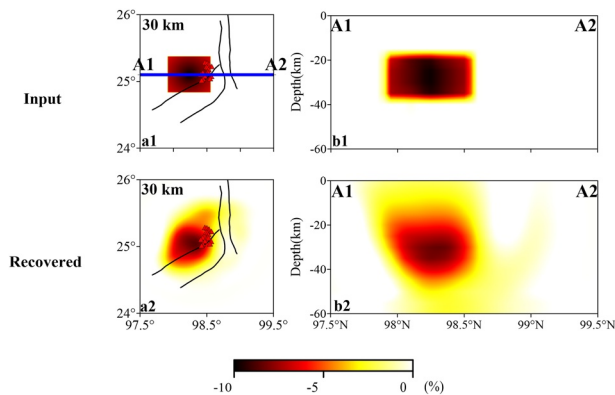


**Figure 9.** Custom resolution test. The input model (a1–b1) is a  $-10\%$  velocity anomaly relative to 1-D regional velocity model of M00 with size of  $0.64^\circ \times 0.52^\circ \times 15$  km at lower crust. The second row (a2–b2) shows anomalies recovered in adjoint tomography. The red triangles are the locations of the volcanoes, and black lines represent the major faults.

The estimated melt fraction here agrees well with the notion that the lower crustal magmatic system is dominated by mush, a state with melt and other fluids distributed within the crystalline framework (Schmandt et al., 2019; Sparks et al., 2019). Other pore-fluids, such as water and  $\text{CO}_2$ , are not taken into consideration in the calculation for melt fraction, as they have stronger effects on compression wave than shear wave velocity (Chu et al., 2010; Huang, Lin, et al., 2015). Annual  $\text{CO}_2$  emission as much as  $4.48\text{--}7.05 \times 10^9$  kg/yr from the TCV (M. Zhang et al., 2016) also implies a substantial contribution of the large lower crustal magma reservoir.

In the uppermost mantle, significant low velocities are imaged at depths of  $\sim 40\text{--}50$  km beneath the GLGSZ to the east of the TCV. A shear velocity of  $3.8\text{--}4.0$  km/s clearly indicates the presence of partial melt. Melt percentage is then inferred based on an uppermost mantle peridotite-basalt melt system using the similar relationship used to estimate the melt fraction in the lower crust (Takei, 2002) (Table S3). Finally, low shear velocities of  $3.8\text{--}4.0$  km/s in the uppermost mantle correspond to  $4\%\text{--}6\%$  melt fraction. Note that this is also a conservative estimation as is showed from resolution tests.

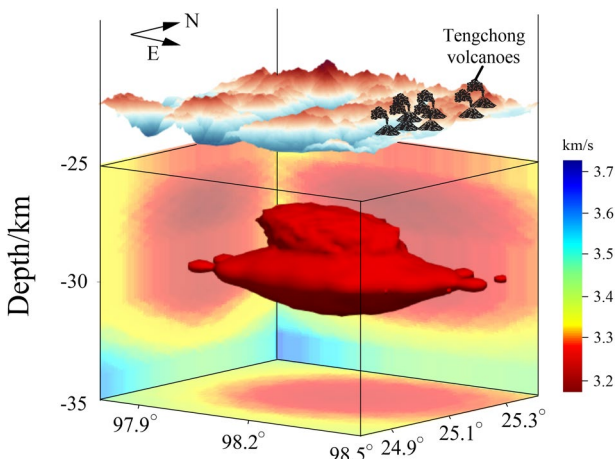


**Figure 10.** 3-D contour of the  $3.25$  km/s velocity as a volume of  $\sim 7,000$  km<sup>3</sup> in the mid-to lower crust. The slices of the magma reservoir in three directions are projected to the surfaces of the box. Topography is plotted above the contour, and the black symbols denote the locations of the volcanoes.

the Supporting Information S1). Then, we find that a S-wave velocity of  $3.25$  km/s in the mid-to-lower crust represents a  $\sim 2\text{--}4.5\%$  basaltic melt fraction.

Here, we use a  $3.25$  km/s contour to outline the magma reservoir in the middle/lower crust (Figure 10) as the LVZ body with a  $V_s$  lower than  $3.25$  km/s containing a significant amount of melt. Subsequently, the total volume of this reservoir is estimated to be over  $7,000$  km<sup>3</sup>. With a  $\sim 2\text{--}4.5\%$  basaltic melt fraction of the reservoir, the potential melt volume is conservatively estimated to be  $140\text{--}315$  km<sup>3</sup>. It should be noted that melt fraction as well as melt volume here could be underestimated since resolution tests show an overall underestimation of low velocity in the mid-to-lower crust. Nevertheless, the estimated melt volume of the TCV is  $\sim 1/6\text{--}1/3$  of the Yellowstone Supervolcano ( $\sim 900$  km<sup>3</sup> from Huang, Lin, et al., 2015), one of the largest and most dangerous supervolcanos on the Earth. And the melt volume ratio of these two volcanoes is also comparable to the annual  $\text{CO}_2$  emission ratio of  $\sim 1/4\text{--}1/2$  between the TCV ( $4.48\text{--}7.05 \times 10^9$  kg) and Yellowstone Supervolcano ( $1.642 \times 10^{10}$  kg).

Here, the uppermost mantle large-scale low-velocity zone beneath the GLGSZ represents mantle upwelling, which supplies the lower crustal magma reservoir and finally fuels the TCV. High  $^3\text{He}/^4\text{He}$  ratios in the TCV basaltic lavas also imply a mantle source of volcanic rocks (C. P. Zhao et al., 2012).

#### 4.2. Multi-Level Magma Plumbing System of the Tengchong Volcano

A recent magnetotelluric (MT) study (Ye et al., 2018) has identified three separate small-scale shallow magma bodies right beneath the TCV in the upper-to mid-crust ( $10\text{--}20$  km depths). These small and shallow magma bodies are, however, below the resolution limit of our adjoint tomography due to the limitation of our seismic station density. These shallow magma bodies are much smaller in scales and are distinct from the larger and deeper magma reservoir imaged by this study. The shallow small magma bodies may represent intermediate to silicic magma chambers. Based on the resistivity value of the magma body, Ye et al. (2018) estimate that these bodies have a minimum of  $\sim 6\%$  melt fraction. If so, then these shallow magma chambers may contain a volume of  $\sim 60$  km<sup>3</sup> intermediate to felsic melt.

Based on these observations, we suggest a multi-level magma plumbing system beneath the TCV, similar to those of the Yellowstone (Huang, Lin, et al., 2015) and Long Valley calderas (Flinders et al., 2018) revealed by recent seismic tomographic studies. Previous teleseismic body tomography reveals a plume-like upwelling from the mantle transition zone or even deeper beneath the TCV (Huang, Wang, et al., 2015; Lei & Zhao, 2016). When the deep upwelling from the mantle transition zone (or even deeper) reaches a shallow upper mantle depth, it starts to partially melt, generating basaltic melt in the uppermost mantle beneath the GLGSZ. The deep-rooted strike-slip faults zone may act as a pathway that transports basaltic melts from the uppermost mantle to the lower crustal magma reservoir.

The ponding of the basaltic melt in the mid/lower crustal magma reservoir may induce partial melting of the mid/lower crust, generating intermediate to silicic magma. Meanwhile, magma fractionation takes place within the magma reservoir (Cashman et al., 2017; Sparks et al., 2019). This fractionation process further generates intermediate to silicic magma that rises to the upper crust along various branches of GLGSZ, forming the isolated upper crustal magma chambers. Geochemical and petrological studies suggested that magma from the enriched upper mantle repeatedly recharges the lower crust and the mafic magma in the lower crust undergoes various degrees of crustal evolution before eruption (Li et al., 2012). Thus, the secular evolution of melt in the multi-level magmatic system from the uppermost mantle to the shallow crust beneath the TCV provides a plausible explanation for the compositional trend from basaltic to andesitic rocks through time (Jiang, 1998; Tucker et al., 2013; Y. Wang et al., 2007).

In summary, our high resolution 3-D S-wave velocity model reveals a multi-leveled magmatic system beneath the TCV. The various degree of melt fraction in the magmatic system indicates the presence of compositional differentiation. However, higher resolution upper crustal imaging based on a denser seismic array is needed in a future study to better image the connection between the lower crustal mafic magma reservoir and the upper crust intermediate to silicic magma chambers.

## 5. Conclusions

We construct a high-resolution 3D crustal model of the TCV using ambient noise adjoint tomography. The 3-D shear velocity model reveals a crustal magma reservoir at a depth of 20–35 km, located to the west of TCV. The basaltic melt fraction in the crustal magma reservoir is estimated to be ~2%–4.5%. In the uppermost mantle, we also observe a large-scale LVZ right beneath the GLGSZ, supplying the magma to the lower crustal magma reservoir. Combining the results from a previous MT study, our tomographic model provides seismic evidence for a multi-leveled volcanic plumbing system of the TCV.

## Data Availability Statement

The ambient noise data of ChinArray-Himalaya I project were provided by China Seismic Array Data Management Center at Institute of Geophysics, China Earthquake Administration (ChinArray DMC, doi:10.12001/ChinArray.Data), which can be accessed from <http://www.chinarraydmc.cn/>. The SEM code is available at <https://geodynamics.org/cig/software/specfem3d/>. The ambient noise adjoint tomography SPECFEM3D\_ANAT package is available from <http://doi.org/10.5281/zenodo.4922092>.

## References

- Amante, C., & Eakins, B. W. (2009). *ETOPO1 1 arc-minute global relief model: Procedures, data sources and analysis*. Boulder, CO: National Geophysical Data Center, NESDIS, NOAA, U.S. Department of Commerce.
- Bensen, G., Ritzwoller, M. H., Barmin, M. P., Levshin, A. L., Lin, F., Moschetti, M. P., et al. (2007). Processing seismic ambient noise data to obtain reliable broad-band surface wave dispersion measurements. *Geophysical Journal International*, 169, 1239–1260. <https://doi.org/10.1111/j.1365-246x.2007.03374.x>
- Cashman, K. V., Sparks, R. S., & Blundy, J. D. (2017). Vertically extensive and unstable magmatic systems: A unified view of igneous processes. *Science*, 355, eaag3055. <https://doi.org/10.1126/science.aag3055>
- Chen, M., Huang, H., Yao, H., van der Hilst, R., & Niu, F. (2014). Low wave speed zones in the crust beneath SE Tibet revealed by ambient noise adjoint tomography. *Geophysical Research Letters*, 41, 334–340. <https://doi.org/10.1002/2013gl058476>
- Christensen, N. I. (1996). Poisson's ratio and crustal seismology. *Journal of Geophysical Research*, 101, 3139–3156. <https://doi.org/10.1029/95jb03446>
- Chu, R., Helmberger, D. V., Sun, D., Jackson, J. M., & Zhu, L. (2010). Mushy magma beneath Yellowstone. *Geophysical Research Letters*, 37, L01306. <https://doi.org/10.1029/2009gl01656>

## Acknowledgments

The authors thank all the people who had participated in the fieldwork of the ChinArray-Himalaya I project. This study is supported by the National Science Foundation of China (grants 41974052; 41774052) and Science, Technology and Innovation Commission of Shenzhen Municipality (JCYJ20190809143817880). Z. Guo would like to thank for support from Center for Computational Science and Engineering at Southern University of Science and Technology. The final 3D velocity model is available at <https://zenodo.org/record/4021704#.X1mdmsg-zZaQ> (10.5281/zenodo.4021704). K. Wang and Y. Yang is supported by Australian Research Council Discovery Project (DP190102940). This is contribution 1666 from the ARC Center of Excellence for Core to Crust Fluid Systems (<http://www.cfs.mq.edu.au>) and 1467 in the GEMOC Key Center (<http://www.gemoc.mq.edu.au>).

- Ding, Z., & Wu, Z. (2013). Advances of ChinArray program. In *Paper presented at 2013 AGU Fall Meeting*. San Francisco, CA. American Geophysical Union.
- Fichtner, A., Kennett, B. L., Igel, H., & Bunge, H. P. (2010). Full waveform tomography for radially anisotropic structure: New insights into present and past states of the Australasian upper mantle. *Earth and Planetary Science Letters*, 290, 270–280. <https://doi.org/10.1016/j.epsl.2009.12.003>
- Flinders, A. F., Shelly, D. R., Dawson, P. B., Hill, D. P., Tripoli, B., & Shen, Y. (2018). Seismic evidence for significant melt beneath the long valley caldera, California, USA. *Geology*, 46, 799–802. <https://doi.org/10.1130/g45094.1>
- Gao, H., & Shen, Y. (2014). Upper mantle structure of the Cascades from full-wave ambient noise tomography: Evidence for 3D mantle upwelling in the back-arc. *Earth and Planetary Science Letters*, 309, 222–233. <https://doi.org/10.1016/j.epsl.2014.01.012>
- Guo, Z., Chen, Y. J., Ning, J., Yang, Y., Afonso, J. C., & Tang, Y. (2016). Seismic evidence of on-going sublithosphere upper mantle convection for intra-plate volcanism in Northeast China. *Earth and Planetary Science Letters*, 433, 31–43. <https://doi.org/10.1016/j.epsl.2015.09.035>
- Hu, J., Song, X.-Y., He, H.-L., Zheng, W.-Q., Yu, S.-Y., Chen, L.-M., & Lai, C.-K. (2018). Constraints of texture and composition of clinopyroxene phenocrysts of Holocene volcanic rocks on a magmatic plumbing system beneath Tengchong, SW China. *Journal of Asian Earth Sciences*, 154, 342–353. <https://doi.org/10.1016/j.jseas.2017.12.029>
- Huang, H. H., Lin, F.-C., Schmandt, B., Farrell, J., Smith, R. B., & Tsai, V. C. (2015). The Yellowstone magmatic system from the mantle plume to the upper crust. *Science*, 348, 773–776. <https://doi.org/10.1126/science.aaa5648>
- Huang, Z., Wang, L., Xu, M., Zhao, D., Mi, N., & Yu, D. (2019). P and S wave tomography beneath the SE Tibetan Plateau: Evidence for lithospheric delamination. *Journal of Geophysical Research: Solid Earth*, 124, 10292–10308. <https://doi.org/10.1029/2019jb017430>
- Huang, Z., Wang, P., Xu, M., Wang, L., Ding, Z., Wu, Y., et al. (2015). Mantle structure and dynamics beneath SE Tibet revealed by new seismic images. *Earth and Planetary Science Letters*, 411, 100–111. <https://doi.org/10.1016/j.epsl.2014.11.040>
- Ji, J. Q., Zhong, D., Sang, H., Qiu, J., & Hu, S. (2000). Dating of two metamorphic events on the basalt granulite from the Nabang area on the border of China and Burma. *Acta Petrologica Sinica*, 16, 227–232.
- Jiang, C. (1998). Stages of eruptions of the Tengchong volcanoes. *Journal of Seismological Research*, 21, 309–319.
- Jiang, G. Z., Hu, S., Shi, Y., Zhang, C., Wang, Z., & Hu, D. (2019). Terrestrial heat flow of continental China: Updated dataset and tectonic implications. *Tectonophysics*, 753, 36–48. <https://doi.org/10.1016/j.tecto.2019.01.006>
- Kern, H., & Richter, A. (1981). Temperature derivatives of compressional and shear wave velocities in crustal and mantle rocks at 6 kbar confining pressure. *Journal of Geophysics*, 49, 47–56.
- Komatitsch, D., & Vilotte, J. P. (1998). The spectral element method: An efficient tool to simulate the seismic response of 2D and 3D geological structures. *Bulletin of the Seismological Society of America*, 88, 368–392.
- Lee, S. J., Chen, H.-W., Liu, Q., Komatitsch, D., Huang, B.-S., & Tromp, J. (2008). Three -dimensional simulations of seismic-wave propagation in the Taipei Basin with realistic topography based upon the spectral-element method. *Bulletin of the Seismological Society of America*, 98, 253–264. <https://doi.org/10.1785/0120070033>
- Lei, J., & Zhao, D. (2016). Teleseismic P-wave tomography and mantle dynamics beneath Eastern Tibet. *Geochemistry, Geophysics, Geosystems*, 17, 1861–1884. <https://doi.org/10.1002/2016gc006262>
- Levshin, A. L., & Ritzwoller, M. H. (2001). Automated detection, extraction, and measurement of regional surface waves. In *Monitoring the comprehensive nuclear-test-ban treaty: Surface waves* (pp. 1531–1545). Basel: Birkhäuser. [https://doi.org/10.1007/978-3-0348-8264-4\\_11](https://doi.org/10.1007/978-3-0348-8264-4_11)
- Li, D. P., Luo, Z., Liu, J., Chen, Y., & Jin, Y. (2012). Magma origin and evolution of Tengchong Cenozoic Volcanic Rocks from West Yunnan, China: Evidence from whole rock geochemistry and Nd-Sr-Pb isotopes. *Acta Geologica Sinica*, 86, 867–878.
- Li, S., Guo, Z., Chen, Y. J., Yang, Y., & Huang, Q. (2018). Lithospheric structure of the northern Ordos from ambient noise and teleseismic surface wave tomography. *Journal of Geophysical Research: Solid Earth*, 123, 6940–6957. <https://doi.org/10.1029/2017JB015256>
- Liu, Q., & Tromp, J. (2006). Finite-frequency kernels based on adjoint methods. *Bulletin of the Seismological Society of America*, 96, 2383–2397. <https://doi.org/10.1785/0120060041>
- Liu, Y., Niu, F., Chen, M., & Yang, W. (2017). 3-D crustal and uppermost mantle structure beneath NE China revealed by ambient noise adjoint tomography. *Earth and Planetary Science Letters*, 461, 20–29. <https://doi.org/10.1016/j.epsl.2016.12.029>
- Luo, Y. (2012). *Seismic imaging and inversion based on spectral-element and adjoint methods (PhD thesis)*. Princeton University.
- Luo, Y., Yang, Y., Xu, Y., Xu, H., Zhao, K., & Wang, K. (2015). On the limitations of interstation distances in ambient noise tomography. *Geophysical Journal International*, 201(2), 652–661. <https://doi.org/10.1093/gji/ggv043>
- Montagner, J. P., & Anderson, D. L. (1989). Petrological constraints on seismic anisotropy. *Physics of the Earth and Planetary Interiors*, 54, 82–105. [https://doi.org/10.1016/0031-9201\(89\)90189-1](https://doi.org/10.1016/0031-9201(89)90189-1)
- Schmandt, B., Jiang, C., & Farrell, J. (2019). Seismic perspectives from the western U.S. on magma reservoirs underlying large silicic calderas. *Journal of Volcanology and Geothermal Research*, 384, 158–178. <https://doi.org/10.1016/j.jvolgeores.2019.07.015>
- Shapiro, N. M., Ritzwoller, M. H., Molnar, P., & Levin, V. (2004). Thinning and flow of Tibetan crust constrained by seismic anisotropy. *Science*, 305, 233–236. <https://doi.org/10.1126/science.1098276>
- Snieder, R. (2004). Extracting the Green's function from the correlation of coda waves: A derivation based on stationary phase. *Physical Review E*, 69, 046610. <https://doi.org/10.1103/physreve.69.046610>
- Sparks, R. S. J., Annen, C., Blundy, J. D., Cashman, K. V., Rust, A. C., & Jackson, M. D. (2019). Formation and dynamics of magma reservoirs. *Philosophical Transactions of the Royal Society*, 377, 20180019. <https://doi.org/10.1098/rsta.2018.0019>
- Takei, Y. (2002). Effect of pore geometry on VP/VS: From equilibrium geometry to crack. *Journal of Geophysical Research*, 107, ECV6-1–ECV6-12. <https://doi.org/10.1029/2001jb000522>
- Tape, C., Liu, Q., Maggi, A., & Tromp, J. (2009). Adjoint tomography of the southern California crust. *Science*, 325, 988–992. <https://doi.org/10.1126/science.1175298>
- Tape, C., Liu, Q., Maggi, A., & Tromp, J. (2010). Seismic tomography of the southern California crust based on spectral-element and adjoint methods. *Geophysical Journal International*, 180, 433–462. <https://doi.org/10.1111/j.1365-246x.2009.04429.x>
- Tromp, J., Komatitsch, D., & Liu, Q. (2008). Spectral-element and adjoint methods in seismology. *Communications in Computational Physics*, 3, 1–32.
- Tromp, J., LuoHanasoge, Y. S., Peter, D., & Peter, D. (2010). Noise cross-correlation sensitivity kernels. *Geophysical Journal International*, 183, 791–819. <https://doi.org/10.1111/j.1365-246x.2010.04721.x>
- Tromp, J., Tape, C., & Liu, Q. (2005). Seismic tomography, adjoint methods, time reversal and banana-donut kernels. *Geophysical Journal International*, 160, 195–216.
- Tucker, R., Zou, H., Fang, Q., & Schmitt, A. (2013). Ion microprobe dating of zircons from active Dayingshan volcano, Tengchong, SE Tibetan Plateau: Time scale and nature of magma chamber storage. *Lithos*, 172–173, 214–221. <https://doi.org/10.1016/j.lithos.2013.04.017>

- Wang, K., Liu, Q., & Yang, Y. J. (2019). Three-dimensional sensitivity kernels for multicomponent empirical green's functions from ambient noise: Methodology and application to adjoint tomography. *Journal of Geophysical Research: Solid Earth*, 124, 5794–5810. <https://doi.org/10.1029/2018jb017020>
- Wang, K., Yang, Y., Basini, P., Tong, P., Tape, C., & Liu, Q. (2018). Refined crustal and uppermost mantle structure of southern California by ambient noise adjoint tomography. *Geophysical Journal International*, 215, 844–863. <https://doi.org/10.1093/gji/ggy312>
- Wang, Y., Zhang, X., Jiang, C., Wei, H., & Wan, J. (2007). Tectonic controls on the late Miocene-Holocene volcanic eruptions of the Tengchong volcanic field along the southeastern margin of the Tibetan plateau. *Journal of Asian Earth Sciences*, 30, 375–389. <https://doi.org/10.1016/j.jseas.2006.11.005>
- Yang, Y., Ritzwoller, M. H., Levshin, A. L., & Shapiro, N. M. (2007). Ambient noise Rayleigh wave tomography across Europe. *Geophysical Journal International*, 168, 259–274. <https://doi.org/10.1111/j.1365-246x.2006.03203.x>
- Yao, H., Beghein, C., & van der Hilst, R. D. (2008). Surface wave array tomography in SE Tibet from ambient seismic noise and two-station analysis: II. Crustal and upper-mantle structure. *Geophysical Journal International*, 163, 205–219. <https://doi.org/10.1111/j.1365-246x.2007.03696.x>
- Yao, H., & Van Der Hilst, R. D. (2009). Analysis of ambient noise energy distribution and phase velocity bias in ambient noise tomography, with application to SE Tibet. *Geophysical Journal International*, 179, 1113–1132. <https://doi.org/10.1111/j.1365-246x.2009.04329.x>
- Ye, T., Huang, Q., Chen, X., Zhang, H., John Chen, Y., Zhao, L., & Zhang, Y. (2018). Magma chamber and crustal channel flow structures in the Tengchong volcano area from 3-D MT inversion at the intracontinental block boundary southeast of the Tibetan Plateau. *Journal of Geophysical Research: Solid Earth*, 123, 11112–11126. <https://doi.org/10.1029/2018jb015936>
- Yu, H., Lin, C., Shi, L., Xu, J., & Chen, X. (2010). Characteristics and origin of mafic and ultramafic xenoliths in trachyandesite lavas from Heikongshan volcano, Tengchong, Yunnan Province, China. *Science China Earth Sciences*, 53, 1295–1306. <https://doi.org/10.1007/s11430-010-4044-6>
- Zhang, B., Zhang, J., Zhong, D., Yang, L., Yue, Y., & Yan, S. (2012). Polystage deformation of the Gaoligong metamorphic zone: Structures, 40Ar/39Ar mica ages and tectonic implications. *Journal of Structural Geology*, 37, 1–18. <https://doi.org/10.1016/j.jsg.2012.02.007>
- Zhang, C., Yao, H., Liu, Q., Zhang, P., Yuan, Y. O., Feng, J., & Fang, L. (2018). Linear array ambient noise adjoint tomography reveals intense crust mantle interactions in North China craton. *Journal of Geophysical Research: Solid Earth*, 123, 368–383. <https://doi.org/10.1002/2017jb015019>
- Zhang, G., & Lei, J. (2015). Mechanism of the 2011 Tengchong, Yunnan, Ms5.2 double earthquakes. *Chinese Journal of Geophysics*, 58, 1194–1204.
- Zhang, M., Guo, Z., Sano, Y., Zhang, L., Sun, Y., Cheng, Z., & Yang, T. F. (2016). Magma-derived CO<sub>2</sub> emissions in the Tengchong volcanic field, SE Tibet: Implications for deep carbon cycle at intra-continental subduction zone. *Journal of Asian Earth Sciences*, 127, 76–90. <https://doi.org/10.1016/j.jseas.2016.06.009>
- Zhao, C. P. (2008). *Mantle-derived helium release characteristics and deep magma chamber activities of present day in Tengchong volcanic area (PhD dissertation) (in Chinese)*. Beijing, China: Institute of Geology, China Earthquake Administration.
- Zhao, C. P., Ran, H., & Chen, K. H. (2011). Present-day temperatures of magma chambers in the crust beneath Tengchong volcanic field, southwestern China: Estimation from carbon isotopic fractionation between CO<sub>2</sub> and CH<sub>4</sub> of free gases escaped from thermal springs. *Acta Petrologica Sinica*, 27, 2883–2897.
- Zhao, C. P., Ran, H., & Wang, Y. (2012). Present-day mantle-derived helium release in the Tengchong volcanic field, Southwest China: Implications for tectonics and magmatism. *Acta Petrologica Sinica*, 28, 1189–1204.
- Zhao, Y., Guo, L., Guo, Z., Chen, Y. J., Shi, L., & Li, Y. (2020). High resolution crustal model of SE Tibet from joint inversion of seismic P-wave travel-times and Bouguer gravity anomalies and its implication for the crustal channel flow. *Tectonophysics*, 792, 228580. <https://doi.org/10.1016/j.tecto.2020.228580>
- Zheng, C., Ding, Z. F., & Song, X. D. (2016). Joint inversion of surface wave dispersion and receiver functions for crustal and uppermost mantle structure in Southeast Tibetan Plateau. *Chinese Journal of Geophysics*, 59, 3223–3236.
- Zhou, Y., Dahlen, F., & Nolet, G. (2004). Three-dimensional sensitivity kernels for surface wave observables. *Geophysical Journal International*, 158, 142–168. <https://doi.org/10.1111/j.1365-246x.2004.02324.x>
- Zhu, H., Bozd  g, E., & Tromp, J. (2015). Seismic structure of the European upper mantle based on adjoint tomography. *Geophysical Journal International*, 201, 18–52. <https://doi.org/10.1093/gji/ggu492>
- Zou, H., Shen, C. C., Fan, Q., & Lin, K. (2014). U-series disequilibrium in young Tengchong volcanics: Recycling of mature clay sediments or mudstones into the SE Tibetan mantle. *Lithos*, 192, 132–141. <https://doi.org/10.1016/j.lithos.2014.01.017>

## References From the Supporting Information

- Christensen, N. I., & Mooney, W. D. (1995). Seismic velocity structure and composition of the continental crust: A global view. *Journal of Geophysical Research*, 100, 9761–9788. <https://doi.org/10.1029/95jb00259>
- Clark, A. N., & Leshner, C. E. (2017). Elastic properties of silicate melts: Implications for low velocity zones at the lithosphere-asthenosphere boundary. *Science Advances*, 3, e1701312. <https://doi.org/10.1126/sciadv.1701312>
- Kennett, B. L. N., & Engdahl, E. R. (1991). Traveltimes for global earthquake location and phase identification. *Geophysical Journal International*, 105, 429–465. <https://doi.org/10.1111/j.1365-246x.1991.tb06724.x>
- Murase, T., & McBirney, A. R. (1973). Properties of some common igneous rocks and their melts at high temperatures. *The Geological Society of America Bulletin*, 84, 3563–3592. [https://doi.org/10.1130/0016-7606\(1973\)84<3563:poscir>2.0.co;2](https://doi.org/10.1130/0016-7606(1973)84<3563:poscir>2.0.co;2)